Research in Astron. Astrophys. **2011** Vol.**11** No. **3**, 245–270
http://www.raa-journal.org *http://www.iop.org/journals/raa*

***R**esearch in*
***A**stronomy and*
***A**strophysics*

Low-ionization galaxies and evolution in a pilot survey up to $z = 1$ *

Edmond Giraud[1], Qiu-Sheng Gu[2], Jorge Melnick[3], Hernan Quintana[4], Fernando Selman[3], Ignacio Toledo[4] and Paula Zelaya[4]

[1] LPTA, Université Montpellier 2 - CNRS/IN2P3, 34095 Montpellier, France; *edmond.giraud@lpta.in2p3.fr*
[2] Department of Astronomy, Nanjing University, Nanjing 210093, China; *qsgu@nju.edu.cn*
[3] European Southern Observatory, Alonso de Córdova 3107, Santiago, Chile
[4] Department of Astronomy and Astrophysics, P. Universidad Catolica de Chile, Casilla 306, Santiago, Chile

Received 2010 June 12; accepted 2010 November 8

Abstract We present galactic spectroscopic data from a pencil beam of $10.75' \times 7.5'$ centered on the X-ray cluster RXJ0054.0–2823 at $z = 0.29$. We study the spectral evolution of galaxies from $z = 1$ down to the cluster redshift in a magnitude-limited sample at $R \leq 23$, for which the statistical properties of the sample are well understood. We divide emission-line galaxies into star-forming galaxies, Low Ionization Nuclear Emission line Regions (LINERs), and Seyferts by using emission-line ratios of [OII], Hβ, and [OIII], and derive stellar fractions from population synthesis models. We focus our analysis on absorption and low-ionization galaxies. For absorption-line galaxies, we recover the well-known result that these galaxies have had no detectable evolution since $z \sim 0.6 - 0.7$, but we also find that in the range $z = 0.65 - 1$, at least 50% of the stars in bright absorption systems are younger than 2.5 Gyr. Faint absorption-line galaxies in the cluster at $z = 0.29$ also had significant star formation during the previous $2 - 3$ Gyr, but their brighter counterparts seem to be only composed of old stars. At $z \sim 0.8$, our dynamically young cluster had a truncated red-sequence. This result seems to be consistent with a scenario where the final assembly of E/S0 took place at $z < 1$. In the volume-limited range $0.35 \leq z \leq 0.65$, we find that 23% of the early-type galaxies have LINER-like spectra with Hβ in absorption and have a significant component of A stars. The vast majority of LINERs in our sample have significant populations of young and intermediate-aged stars and are thus not related to AGNs, but to the population of 'retired galaxies' recently identified by Cid Fernandes et al. in the Sloan Digital Sky Survey (SDSS). Early-type LINERs with various fractions of A stars and E+A galaxies appear to play an important role in the formation of the red sequence.

Key words: cosmology: observations — galaxies: evolution — large scale structures — evolution — RX J0054.0–2823

∗ Supported by the National Natural Science Foundation of China.

1 INTRODUCTION

In the course of an investigation of the diffuse intergalactic light in X-ray emitting clusters at intermediate redshifts (Melnick et al. 1999), we detected a puzzling S-shaped arc-like structure in the ROSAT cluster RX J0054.0–2823 (Faure et al. 2007), which we tentatively identified as the gravitationally lensed image of a background galaxy at a redshift between $z = 0.5$ and $z = 1.0$. The cluster, however, is characterized by having three dominant D or cD galaxies in the center, two of which are clearly interacting. We designed an observing strategy that allowed us to simultaneously observe the arc, the diffuse Intra-Cluster Light (ICL), and a magnitude limited sample of individual galaxies in the field by taking advantage of the multi-object spectroscopic mode of the FORS2 instrument on Paranal. By optimizing the mask design (see below), we were able to obtain: (a) very deep observations of the arc; (b) very deep long-slit observations of the ICL; and (c) redshifts and flux distributions for 654 galaxies, of which 550 are in the pencil beam and at $0.275 \leq z \leq 1.05$.

Our pencil beam sample covers a redshift range up to $z = 1$ (with some galaxies up to $z = 1.7$). In standard cosmology with $H_0 = 75\ \mathrm{km\ s^{-1}\ Mpc^{-1}}$, $\Omega_{0,m} = 0.30$, and $\Omega_{0,\Lambda} = 0.70$, this range provides large leverage of about 3000 Mpc or 7 Gyr, which should be sufficient to extract some of the most conspicuous characteristics of galaxy evolution at $z \leq 1$. About half of all stars seem to still be forming, mostly in disks, in this redshift range (Dickinson et al. 2003; Hammer et al. 2005). Our spectroscopy provides a 50%–60% complete sample of the galaxies in a pencil beam of $\sim 10' \times 10'$, centered on the cluster, uniformly down to $R = 23$. Our sample is comparable in size with the DEEP1 spectroscopic pilot survey (Weiner et al. 2005), but is smaller than large surveys such as DEEP2 (e.g. Lin et al. 2008; Yan et al. 2009), VVDS (e.g. Franzetti et al. 2007; Garilli et al. 2008), and GOODS (e.g. Bell et al. 2005; Weiner et al. 2006). The advantage of a pilot survey is that it can be handled rather easily by a single (or a few) researcher(s) to test new methods and new ideas before applying these new methods to large samples.

The vast majority of our individual spectra, which were reduced to zero redshift, have S/N ratios per $2.6\,\text{Å}$ pixel larger than 3 at $4200\,\text{Å}$. This resolution is very well-adapted to the detection of small equivalent width [OII] emission, which is expected to be found in bulge dominated galaxies with small disks, in some LINERs, in "mixed" mergers between E/S0 and star-forming objects, and perhaps in some post-starbursts galaxies. The line of sight of our field crosses three main structures: a dynamically young cluster at $z = 0.29$, an overdense region with layers at $z = 0.4 - 0.5$, and a mixed region of the field and possible layers from $z = 0.6$ to $z = 1$. According to morphology-density relations (Dressler 1980; Dressler et al. 1997; Melnick & Sargent 1977; Smith et al. 2005; Postman et al. 2005; Cooper et al. 2006; Scoville et al. 2007), we expect that overdense regions will provide a rather large number of red objects available for study. Therefore, red objects with or without star formation, or with low photo-ionization, are the subject which we will focus on, keeping in mind the possible roles of E+A galaxies (Dressler & Gunn 1983; Norton et al. 2001; Blake et al. 2004; Goto 2007; Yang et al. 2008, and references therein) and of LINERs (Yan et al. 2006) in the building-up of the red sequence.

We focus on galaxies with either low star-formation or low ionization which appear at $z \leq 0.6$. We use a line ratio diagnosis based upon [OII], Hβ, and [OIII], from Yan et al. (2006), to classify galaxies as LINERs, star-forming galaxies, and Seyferts. This method, combined with visible morphology, allows us to isolate a significant population of early-type LINERs, and galaxies with diluted star-formation in later morphological types at $z = 0.35 - 0.6$.

Several studies suggest that the bulk of stars in early-type cluster galaxies formed at a redshift of $z \geq 3$, while those in lower density environments may have formed later, but still at $z \geq 1.5 - 2$ (for reviews see Renzini 2006; Renzini 2007). This may contradict the rise in the number of massive red galaxies found by Faber et al. (2007) who concluded that most early-type galaxies reached their final form below $z = 1$. Our data include a clear red sequence at $z = 0.29$ and quite a large number of absorption systems up to $z \sim 1$, which we fit with population synthesis models in order to search for age variations with z and luminosity.

The paper is structured as follows. Section 2 presents details of the observations and the data reduction procedures. Section 3 is about the resulting redshift catalog. Section 4 presents an overview of variations in spectral energy distribution with redshift for absorption and emission systems. Section 5 is dedicated to population variations with z and luminosity in absorption systems. Low-ionization galaxies are in Section 5.3. In Section 5.4, we suggest a scenario in which early-type LINERs will become E/S0 galaxies once the A stars die and photo-ionization disappears. Summary and conclusions are in Section 6.

2 OBSERVATIONS AND DATA REDUCTION

The observations (ESO program 078A–0456(A)) were obtained with the FORS2 instrument[1] at the Cassegrain focus of the VLT UT1 telescope in multi-object spectroscopy mode with the exchangeable mask unit (MXU). They were acquired in service observing and were spread over the two periods, 78 and 80, to satisfy our observing requirements. FORS2 was equipped with two $2\mathrm{k} \times 4\mathrm{k}$ MIT CCDs with $15\ \mu\mathrm{m}$ pixels. These CCDs have high efficiency in the red combined with very low fringe amplitudes. We used the 300V and 600RI grisms, both with the order sorting filter GG435. With this filter, the 300V grism has a central wavelength at 5950 Å and covers a wavelength between $4450 - 8700$ Å at a resolution of 112 Å mm^{-1}. The 600RI grism has a central wavelength of 6780 Å and covers the 5120–8450 Å region at a resolution of 55 Å mm^{-1}. Combined with a detector used in binned mode, the 300V grism has a pixel resolution of 3.36 Å pixel^{-1}. The grisms were used with a slit width of $1''$. In order to match the major and minor axis of the ICL, and the prominent arc-like feature, rotation angles of $-343°$, $-85°$ and $-55°$ were applied. The slit lengths used for the ICL spectra were $56.5''$, $32.5''$ and $24.5''$, while those of typical galaxies varied between $7''$ and $12''$. The ICL was located either on the master CCD or the secondary one, resulting in a combined pencil beam field of $10.75' \times 7.5'$ (Fig. 1).

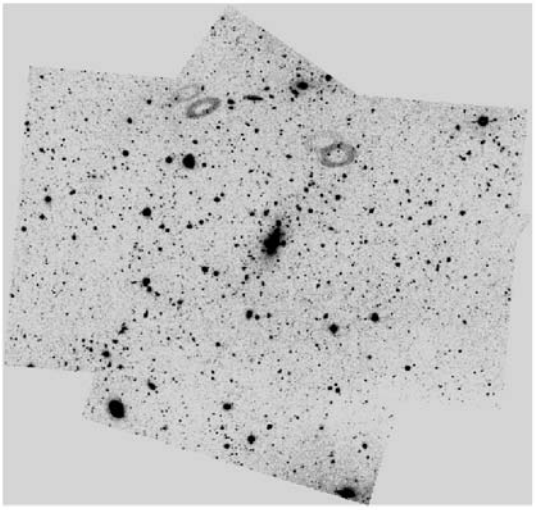

Fig. 1 Central (*pencil beam*) field from R images obtained with the wide field camera at the 2.2 m telescope in La Silla.

[1] FORS1+2 User Manual VLT-MAN-ESO–13100–1543 Issue 4, 2005

A total of 30 hours of observing time, including field acquisition, mask positioning, and integration time, was dedicated to our pencil beam redshift survey of the J0054.0–2823 field. Each mask was filled with $39 - 49$ slitlets in addition to the ICL slits. In order to trace some of the apparent structures connected to J0054.0–2823, and to reach beyond its virial radius, we also obtained MXU exposures of eight FORS2 fields of $7' \times 5'$ adjacent to the pencil beam. In total, we obtained spectra of 730 individual sources.

2.1 Mask Preparation

Tables for preparing the masks and instrument setups were obtained with the FORS Instrumental Mask Simulator[2,3]. The selection of objects for the preparation of slit masks of the pencil beam field was done by using a photometric catalog in V and I, which we derived from deep images obtained in a previous NTT run (Faure et al. 2007), and pre-images in R from the VLT. The selection of objects in fields adjacent to the pencil beam was obtained by using images taken with the WIde Field Imager (WIFI; $34' \times 33'$) on the 2.2 m telescope at La Silla. Photometry in V and R from the WIFI images is used throughout the paper. The allocated time was divided in observing blocks (OBs) to be executed in service mode. A typical OB of 1 h of execution time had a science integration time of 2900 s, used for two exposures of 1450 s.

We estimated exposure times for E to Sb galaxies in the range $z = 0.3 - 0.8$. Using the exposure time calculator of FORS, we obtained magnitude limits, the major steps of which are given in Table 1, which we used to optimize the distribution of slitlets in the masks. After isolating bright objects which did not require long exposure times, we prepared a grid with an exposure time step of 2×1450 s, which we filled with galaxies having V magnitudes such that the expected S/N ratio per pixel would be better than 2.8 (1 pixel along the dispersion). After recording VLT pre-images in the red band, we made a similar grid in R and adjusted the two grids. The masks were prepared interactively with the FIMS tool and the R pre-images. We started to fill masks with objects that required an exposure time $\leq 2 \times 1450$ s, then moved to $\leq 4, 6$, and 8×1450 s. Because we prepared sets of masks with slits in very different directions (in particular, those of the ICL's long and short axis), objects that could not be targeted with a mask in a given direction (i.e. such as any mask with running name ICL-s in Table 2) were targeted in a perpendicular one (i.e. masks with running name ICL-L), an approach which made the mask coverage quite efficient, especially in overdense areas and field edges. Objects which were close to a predicted S/N of 2.8 in an OB were selected to also be observed in another OB as often as possible. Some objects with good expected S/N in an OB were re-observed in another OB when there was no other target in the corresponding slit strip. This approach provided a set of high S/N (~ 20) ratio spectra.

A total of 973 slitlets were selected, 621 in 14 different masks in the pencil beam field, and 352 in 8 masks in the adjacent fields. Thirty-five percent of the sources in the pencil beam field were observed through different masks, whereas the slitlets in the adjacent fields were all for different sources.

Table 1 Table Used for Preparing MXU Plates for Multiple Observing Blocks

Number of OBs of 1 h	Integration time (s)	Magnitude limit in V	S/N for S0-Sb at $0.3 \leq z \leq 0.8$
1	2900	24.4 – 24.8	2.8 – 5.2
2	5800	24.8 – 25.2	2.8 – 5.2
4	11 600	25.2 – 25.6	2.8 – 5.2

[2] *http://www.eso.org/sci/observing/phase2/FORS/FIMS.html*

[3] FORS1+2 FIMS Manual VLT-MAN-ESO–13100–2308 Issue 78, 2006

Table 2 Record of the MXU Observations

Name	OB ID	Date	Exp. time (s)	# slitlets	Grism
Bright1	255728	20 Oct. 06	3×550	34	600RI
Bright2	255726	23 Oct. 06	3×550	38	600RI
SW1	255710	18 Oct. 06	3×550	45	300V
SW2	255708	15 Oct. 06	3×550	40	300V
W	255712	19 Oct. 06	3×550	49	300V
SE	255706	3 Oct. 07	3×550	42	300V
N	255716	5 Oct. 07	3×550	42	300V
NW	255714	5 Oct. 07	3×550	48	300V
NE	255718	14 Oct. 07	3×550	47	300V
E	255704	15 Oct. 06	3×710	39	600RI
ICL-s1	255750	12 Dec. 06	2×1450	46	300V
ICL-s2	255748	15 Nov. 06	2×1450	48	300V
ICL-L1	255761	12 Dec. 07	2×1450	41	300V
ICL-L2	255763	9 Jan. 07	2×1450	39	300V
arc2	255734	24 Nov. 06	2×1450	48	300V
arc1	255736, 38	9 Jan. 07, 11 Sept. 07	4×1450	43	300V
ICL-s3	255744, 46, 47	27 Oct. 06, 9 Nov. 06	6×1450	47	300V
ICL-L3	255752, 59, 60	21 Sept. 07, 31 Oct. 07	6×1450	49	300V
arc3	255730, 32, 33	17 Aug. 07	6×1450	46	300V
ICL-s4	255739, 41, 42, 43	23 Oct. 06, 13 Nov. 06	8×1450	46	300V
ICL-L4	255754, 56, 57, 58	15, 17 & 20 Nov. 06	8×1450	49	300V
RI	255720, 22, 23, 24, 25	13 Nov. 06, 12 & 14 Sept. 07, & 3 Oct. 07	10×1450	47	600RI

The resulting list of masks and OBs, as well as the record of observations, is given in Table 2. Spectra of the pencil beam field were obtained through masks with running names Bright, ICL-L, ICL-s, and arc. ICL-L and ICL-s were obtained with rotator angles -343° and -85° respectively, and an arc with a rotation of -55°. Masks with names SE, E, NE, N, NW, W, SW1 and SW2 were in adjacent fields. The observations were obtained during clear nights, with seeing between $0.7''$ and $1.5''$ and a dark sky.

2.2 Spectral Extraction

The data were reduced by the ESO quality control group who provided us with science products (i.e. sky subtracted, flat fielded and wavelength calibrated spectra of our objects), together with calibration data: master bias (bias and dark levels, read-out noise), master screen flats (high spatial frequency flat, slit function), wavelength calibration spectra from He-Ar lamps, and a set of spectrophotometric standards, which were regularly observed. The sky subtracted and wavelength calibrated 2D spectra allowed a very efficient extraction of about 60% of the spectra. Nevertheless, the pipeline lost a significant fraction of objects, especially when they were located on the edges of the slitlets. To increase the efficiency of the spectral extraction, we performed a new reduction starting from frames that were dark subtracted, flat-fielded and wavelength calibrated, but not sky subtracted, using a list of commands taken from the LONG context of the MIDAS package. For each slitlet, the position of the object's spectrum was estimated by averaging 500 columns in the dispersion direction between the brightest sky lines and measuring the maximum of the resulting profile. The sky background was estimated on one side of the object, or on both, depending on each case. Spatial distortion with respect to the columns was measured on the sky line at 5577 Å and used to build a 2D sky which was subtracted from the 2D spectrum. Multiple exposures were then aligned and median averaged. The 1D spectra of objects were extracted from 2D medians by using the optimal extraction method in MIDAS.

2.3 Redshift Identification

The identification of lines for determining the redshifts was done independently from two methods by three of the authors. The 2D spectrum was visually scanned to search for a break in the continuum, or an emission line candidate (e.g. [OII] λ3728.2 Å). A plot of the 1D spectrum was displayed in the corresponding wavelength region to search for [OII], the Ca H and K lines, and/or Balmer lines Hϵ, H9 λ3835.4 Å, H8 λ3889.1 Å, H10 λ3797.9 Å, and Hδ. The redshift was then confirmed by searching for the [OIII] doublet λ4958.9 and 5006.8 Å, and Hβ in emission if [OII] had been detected, or the G band and the Mgb band, if the 4000 Å break and (or) the H and K lines had been identified. The MgII λ2799 Å line in absorption and, in some cases, AlII λ 3584 Å were searched to confirm a potential redshift $z \geq 0.65$, while in the cases of low redshift candidates, we searched for Hβ, the NaD doublet λ5890 and 5896 Å, and in a few cases Hα. The Hγ line, the E (FeI+CaI λ5270 Å) absorption feature and, in some bright galaxies the Fe λ4383 Å, Ca λ4455 Å, and Fe λ4531 Å absorption lines, were used to improve the redshift value. The resulting identification ratio of galaxy redshifts is on the order of 90%. The 10% of so-called unidentified cases include stars, objects with absorption lines which were not understood, a few objects with low signal, and defects. Six QSOs were also found. An example of a good spectrum of a red galaxy, with its main absorption lines identified, is shown in Figure 2.

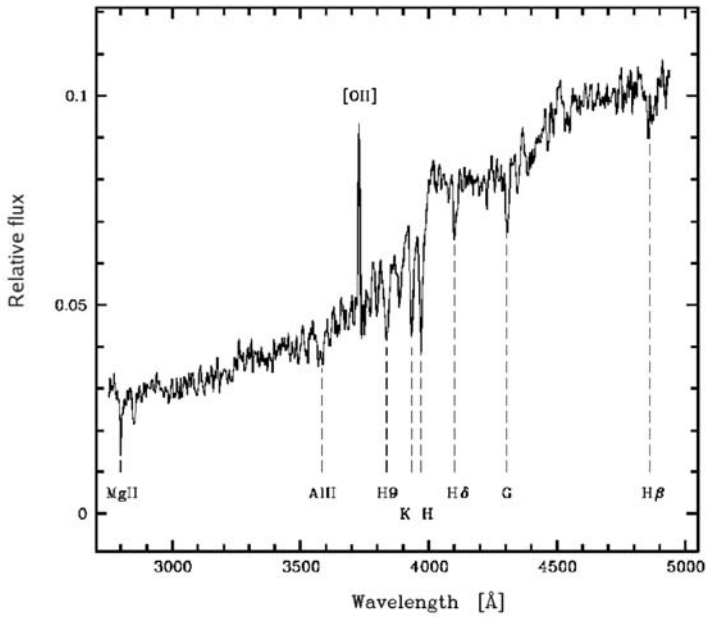

Fig. 2 Example of a spectrum of a red bright galaxy with [OII] and the main absorption lines identified.

A second independent visual identification was performed using Starlink's Spectral Analysis Tool (SPLAT-VO), by matching a Sloan Digital Sky Survey (SDSS) reference table of emission and absorption lines[4] to the spectra. After a first estimate of the redshift, a cross-correlation was performed using the FXCOR task in the RV package of IRAF[5]. Due to the large span of redshifts,

[4] *http://www.sdss.org/dr5/algorithms/linestable.html*

[5] IRAF is distributed by the National Optical Astronomy Observatory, which is operated by the Association of Universities for Research in Astronomy, Inc., under a cooperative agreement with the National Science Foundation.

two sets of templates were used. The first one consisted of three template spectra of galaxies ($\lambda = 3500 - 9000$ Å with emission and absorption lines and a dispersion of 3 Å pix^{-1}) from the SDSS survey[6] with continuum subtraction using a cubic spline order five fitting function. The second set of templates were two average composite spectra of early type and intermediate type galaxies ($\lambda = 2000 - 7000$ Å with only absorption lines and a dispersion of 2 Å pix^{-1}) from the K20 survey[7] using a cubic spline order seven function for continuum subtraction. An interactive selection of the wavelength range used in the cross-correlation was done on each spectrum, avoiding contamination by sky lines. The spectra were re-binned to the template dispersion (smaller for 300V spectra and larger for 600RI spectra), which gave the best results. Velocity errors were determined from the quality of the cross-correlation, by using the standard R value of Tonry & Davies (1979). Here we used $R_{\rm T}$ to differentiate it from the R band magnitude symbol. These values are provided in the IRAF task FXCOR and explained in the quoted reference. In brief, $R_{\rm T}$ is proportional to the ratio of the fitted peak height to the antisymmetric noise as defined by Tonry & Davies (1979).

A third independent visual inspection was carried out when a discrepancy was seen between the previous two sets of measurements, and also in the very few cases were no redshift could be measured. For these spectra, we first tried to detect emission or absorption lines and then used Gaussian fits to establish the line centroids and their errors and shifts. The redshift of each line was measured independently and the galaxy redshift was obtained from the weighted average of all the lines. This third inspection resolved nearly all the few remaining discrepancies, so we have retained the cross-correlation values whenever possible. We note that Xcorr failed in two instances: 1) for $z > 0.8$ galaxies with low S/N and few weak absorption lines, and, 2) when there were no absorption lines, but 1, 2 or 3 clear emission lines, were present. In these cases, we used the visual line identifications and assigned a conservative error of 300 km s^{-1}.

Spectra from more than one mask were obtained for 94 objects. Their final velocities and velocity errors were calculated as error-weighted means from multiple observations, although no significant disagreements were found. These repeated observations serve as a check of the internal errors.

Figure 3 presents the differences between the cross-correlation velocity measurements for all galaxies with multiple observations. The representative full width half maximum (FWHM) error is 200 km s^{-1}. In Figure 4, we have plotted the relation between velocity errors and the Tonry $R_{\rm T}$ value obtained in our cross correlations. Most errors are < 300 km s^{-1} even for $4 > R_{\rm T} > 2$ and the typical error is on the order of 80 km s^{-1}, with the vast majority of the radial velocities having errors below 200 km s^{-1}. We have only discarded a few values with $R_{\rm T} < 1$, when there were no measurable emission lines.

2.4 Flux Calibrations

The 1D spectra were divided by the response curve of the detector, which had been determined from four spectrophotometric standard stars observed during the runs, and reduced by the same method (bias, flat field, wavelength calibration, and extraction) as the galaxy spectra. The thick absorption telluric band of O_2 centered at 7621 Å (unresolved line series) was not removed from the observation response curve and was considered to be a feature of the global wavelength-dependent efficiency.

The relative fluxes per wavelength of the corrected spectra can be compared with stellar population models, in an arbitrary unit, but are not calibrated in flux. The spectra were re-binned to the $z = 0$ rest frame with relative flux conservation. Because a significant fraction of spectra have too low a S/N ratio to make a meaningful comparison with population synthesis models, one may either select the brightest objects or combine spectra of similar types. The spectra taken at different locations of the MXU masks have different lengths along the dispersion direction. In order to merge them, the spectra were normalized to have the same flux in the region 4050–4250 Å (see below).

[6] *http://www.sdss.org/dr2/algorithms/spectemplates/index.html*

[7] *http://www.arcetri.astro.it/∼k20/spe_release_dec04/index.html*

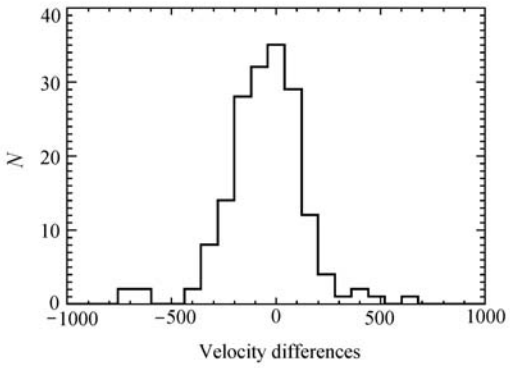

Fig. 3 Occurrence (N) of radial velocity differences for galaxies with multiple observations. The objects with velocity discrepancies larger than $400\,\mathrm{km\ s^{-1}}$ are broad line QSOs and one high-z galaxy.

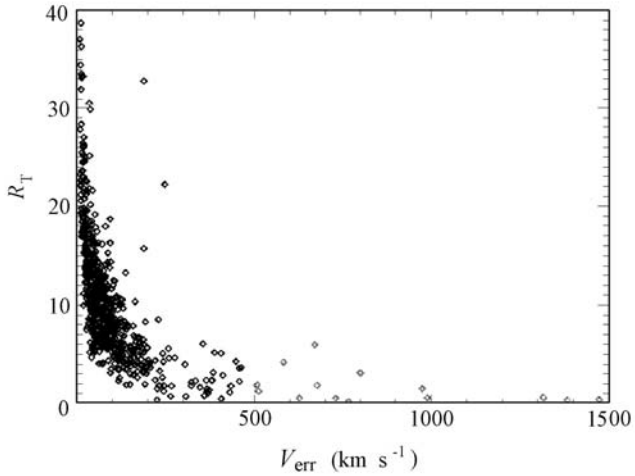

Fig. 4 Relation between radial velocity errors (V_{err}) and the Tonry R_{T} parameter (1979) in redshifts obtained by cross-correlation. The points departing from the general trend (5 points with $R_{\mathrm{T}} > 10$ and five with $V_{\mathrm{err}} > 500\,\mathrm{km\ s^{-1}}$) are five QSOs and distant weak spectrum galaxies with emission lines. Objects with $V_{\mathrm{err}} > 500\,\mathrm{km\ s^{-1}}$, marked in grey, were not used in the combined spectra.

2.5 Quality of the Spectra

The final S/N ratio of the extracted spectra, corrected for the response curve, and re-binned to zero redshift, depends on a number of parameters: seeing, night sky transparency and background, magnitude of the object and integration time, wavelength of the S/N measurement, and redshift. To give an idea of the final products, we present in Table 3 a representative set of 28 spectra at various z, magnitudes, number of OBs and resulting S/N ratio measured on zero redshift spectra in the wavelength range 4150–4250 Å, which corresponds well to the location where we will measure the main indexes of this work. S/N ratios of spectra re-binned to zero redshift are for a pixel element of 2.6 Å throughout the paper. Table 3 also gives the names of the OBs.

Table 3 Signal-to-noise Ratio of Representative Spectra

z	V	R	N(OB)	S/N	Name of OBs	Grism
0.2923	19.2	18.6	2	14	arc1	300V
0.2932	20.3	19.3	2	18	ICL-L1 & L2	300V
0.2928	21.6	20.5	3	17	arc2 & ICL-L1	300V
0.2905	22.8	22.1	2	10	ICL-L1 & L2	300V
0.2910	23.5	22.8	3	9	arc1 & 2	300V
0.4486	21.3	20.0	1	6	Bright2	600RI
0.4477	22.3	21.3	2	20	arc1	300V
0.4148	23.0	22.3	2	7	ICL-s1 & s2	300V
0.4538	23.1	22.0	5	14	ICL-L4 & arc2	300V
0.5355	22.3	20.9	1	8	arc2	300V
0.6309	22.7	21.4	4	11	arc2 & 3	300V
0.6553	22.3	21.5	4	9	ICL-s4 & arc2	300V
0.6282	23.5	22.5	5	9	arc1 & 3	300V
0.6267	23.9	22.9	4	10	arc3	300V
0.6864	22.6	21.9	1	4	ICL-s2	300V
0.6886	23.0	22.0	7	13	ICL-L3 & L4	300V
0.6861	23.0	22.1	4	8	ICL-s4	300V
0.6864	23.5	22.3	4	10	ICL-s3 & arc2	300V
0.6879	23.8	22.8	4	7	ICL-s4	300V
0.8222	20.7	20.0	1	10	ICL-s1	300V
0.8287	22.7	22.4	5	10	ICL-s4 & arc2	300V
0.8249	23.2	22.6	3	8	arc3	300V
0.8823	23.8	23.4	4	3.5	ICL-s4	300V
0.9792	23.3	22.7	3	8	arc3 (*)	300V
0.9626	23.2	22.7	4	5	ICL-L4 (*)	300V
0.9637	23.4	23.2	3	6	ICL-s3	300V
0.9809	23.8	23.7	5	6	RI	600RI
1.0220	24.1	23.3	4	3	ICL-s4	300V

The columns indicate respectively: the redshift (z) of a selected object, its V and R Petrosian magnitudes, the number of observing blocks N(OB) from which its spectrum is extracted, the S/N ratio measured in the wavelength range 4150–4250 Å of the spectrum rebinned to zero redshift, the name of observing blocks from Table 2, and the grism used. Spectra from OBs with the running name "arc" have a higher average S/N ratio than those with the name "ICL" as illustrated by the two objects marked (*).

2.6 Spectral Indexes

The 4000 Å break amplitude definition used in the present paper is the 'narrow' 4000 Å break defined by Balogh et al. (1999) as the flux ratio in the range 4000–4100 Å over 3850–3950 Å (e.g. Kauffmann et al. 2003). The error in D(4000) is calculated from the spectral noise in the two passbands. The equivalent widths of [OII] and of Hδ were measured by using the MIDAS context ALICE as follows: the continuum was obtained by linear interpolation through two passbands on each side of the line, a Gaussian was fitted to the emission or absorption line, and an integration was done over the resulting Gaussian profile above or below the continuum. The continuum and line fits, and the integration, were done interactively in a graphic window in which the spectral region of the line was displayed. Table 4 lists the wavelength ranges of the sidebands used to define the fluxes and continua.

Uncertainties in equivalent widths were deduced from simple Monte Carlo calculations: the values of the equivalent widths are the average of 20 continuum determinations and best Gaussian fits to the absorption or emission lines, and the errors in equivalent widths are deduced from the Monte Carlo dispersion. The largest index errors are for spectra in which Hδ is both in absorption and in emission. In such cases, the emission line was removed after fitting the spectrum of an A star onto all Balmer lines to estimate the depth of Hδ in absorption, and this step was added to the Monte

Table 4 Wavelength bands used in the measurement of the 4000 Å break amplitude, and in the determination of the continua of the [OII] and Hδ indexes (equivalent widths).

Index	Blue band [Å]	Red band [Å]
D(4000)	3850–3950	4000–4100
EQW([OII])	3650–3700	3750–3780
EQW(Hδ)	4030–4070	4130–4180

Carlo simulation. The errors of indexes given in tables of combined spectra throughout the paper are those which were measured on the combined spectra. They do not take into account the astrophysical dispersions in the distributions of individual galaxies which were used to build combined spectra. Those astrophysical dispersions are given in relevant tables concerning spectral variations.

Full observational measurement errors on indexes of individual spectra were obtained by measuring $\mathrm{D}(4000)$ and EQW([OII]) on spectra with multiple observations. Thus 17% of the spectra have typical errors of 4% in D(4000) and 10% in EQW([OII]); 54% have typical errors of 8% in D(4000) and 20% in EQW([OII]); and 14% have poorer spectra with typical errors of 16% in D(4000) and 40% in EQW([OII]).

2.7 Stellar Population Analysis

In order to study the stellar population quantitatively, we applied a modified version of the spectral population synthesis code, *starlight*[8] (Cid Fernandes et al. 2004; Gu et al. 2006) to fit the observed and combined spectra. The code does a search for the best-fitting linear combination of 45 simple stellar populations (SSPs), 15 ages, and 3 metallicities ($0.2\,Z_\odot$, $1\,Z_\odot$, $2.5\,Z_\odot$) provided by (Bruzual & Charlot 2003) to match a given observed spectrum O_λ. The model spectrum M_λ is

$$M_\lambda(x, M_{\lambda_0}, A_V, v_\star, \sigma_\star) = M_{\lambda_0}\left[\sum_{j=1}^{N_\star} x_j b_{j,\lambda} r_\lambda\right] \otimes G(v_\star, \sigma_\star), \tag{1}$$

where $b_{j,\lambda} = L_\lambda^{\mathrm{SSP}}(t_j, Z_j)/L_{\lambda_0}^{\mathrm{SSP}}(t_j, Z_j)$ is the spectrum of the j^{th} SSP normalized at λ_0, $r_\lambda = 10^{-0.4(A_\lambda - A_{\lambda_0})}$ is the reddening term, x is the population vector, M_{λ_0} is the synthetic flux at the normalization wavelength, and $G(v_\star, \sigma_\star)$ is the line-of-sight stellar velocity distribution modeled as a Gaussian centered at velocity $v_\star$ and broadened by $\sigma_\star$. The match between model and observed spectra is calculated as

$$\chi^2(x, M_{\lambda_0}, A_V, v_\star, \sigma_\star) = \sum_{\lambda=1}^{N_\lambda} \left[(O_\lambda - M_\lambda)\, w_\lambda\right]^2,$$

where the weight spectrum w_λ is defined as the inverse of the noise in O_λ. The code yields a table with input and output parameters for each component. Input parameters include individual stellar masses, ages, metallicities, L/M, and so on, and output parameters include luminosity fractions, mass fractions, fit parameters of individual components and so on, and global parameters such as velocity dispersion and extinction. For more details, we refer the reader to the paper (Cid Fernandes et al. 2005). In the present work, we use the standard luminosity fraction in the rest frame of normalized spectra at 4050 Å, which we compare in different redshift bins.

Figure 5 shows an example of the fit for the averaged spectrum at $\langle z\rangle = 0.29$. Panels (a), (b) and (c) correspond to absorption line, emission line, and all spectra, respectively. After fitting the

[8] *http://www.starlight.ufsc.br/*

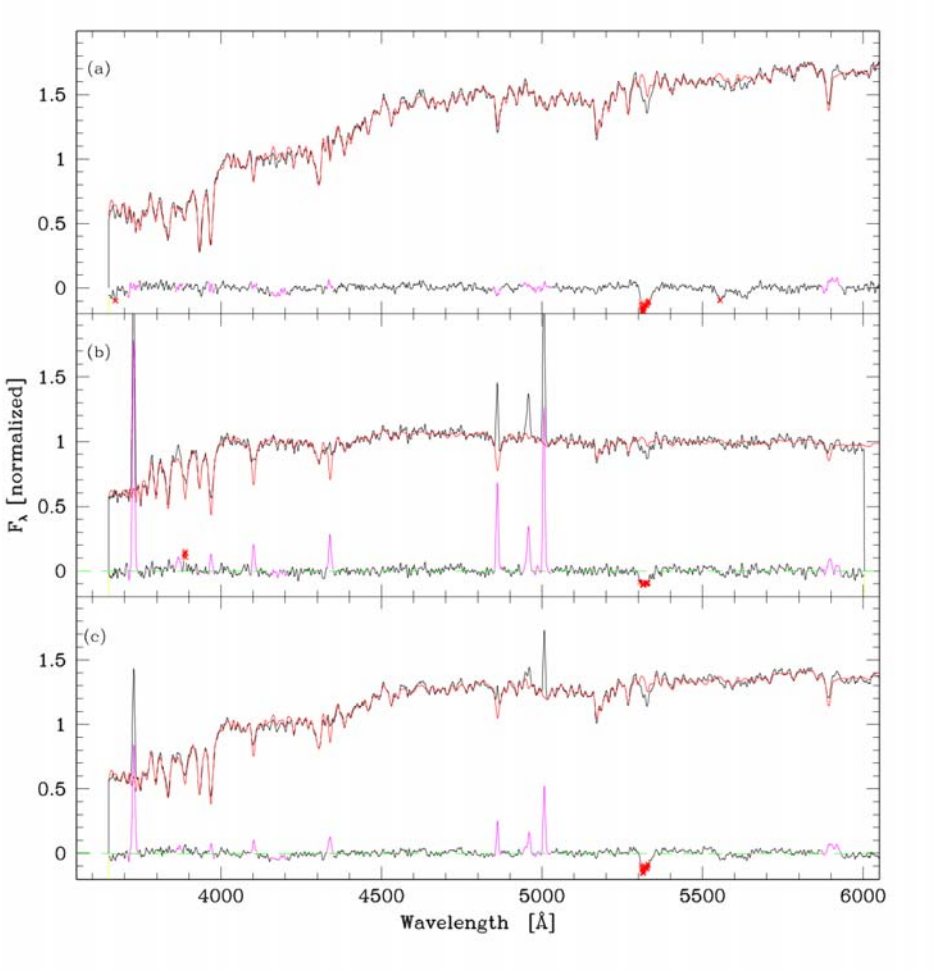

Fig. 5 Spectral fitting results with SSP models for the redshift $\langle z \rangle = 0.29$ bin. (a) Observed (*thin black line*), model (*red line*; color online) and residuals for the absorption spectrum. Points indicate bad pixels and emission line windows that were masked out during fitting. (b) Emission line spectrum; (c) Total spectrum.

spectra, we rebin the 45 SSPs into five components according to their age: I ($10^6 \leq t < 10^8$ yr), II ($10^8 \leq t < 5 \times 10^8$ yr), III ($5 \times 10^8 \leq t < 10^9$ yr), IV ($10^9 \leq t < 2.5 \times 10^9$ yr) and V ($t \geq 2.5 \times 10^9$ yr). Components with the same age and different metallicities are combined together.

3 CATALOG OF GALAXIES AND LARGE SCALE STRUCTURES IN THE LINE OF SIGHT IN THE PENCIL BEAM

Table 5 presents positions, redshifts, Petrossian R-magnitudes (m_R), radial velocities and the corresponding measurement errors, $R_{\rm T}$ values, and line identifications for the full sample of 654 galaxies observed in our program. The full catalog, from which Table 5 is extracted, will be sent as a public database to CDS. The rough data are presently stored in the public domain at ESO.

Table 5 Properties of Galaxies in the Field of RX J0054.0–2823

Obj	RA (α) J2000	Dec. (δ) J2000	z	m_R	V (km s^{-1})	$V_{\rm err}$ (km s^{-1})	$R_{\rm T}$	Lines
23	13.598707	–28.434965	0.79304	22.78	237912	161	4.7	K–H
26	13.590379	–28.416917	0.77636	22.26	232908	77	8.1	[OII]–H10–H9–H
27	13.584442	–28.394515	0.41463	22.29	124389	22	17.3	[OII]–H9–H–Hβ–[OIII]
28	13.586628	–28.438063	0.44877	22.02	134631	73	6.7	K–H–G
30	13.580301	–28.435437	0.29032	21.08	87096	68	11.3	H9–K–H–Hδ–Hα
31	13.572009	–28.380385	0.63267	21.32	189801	49	11.5	[OII]–K–H
32	13.579012	–28.439414	0.45335	—	136005	22	19.5	[OII]–Hγ–Hβ–[OIII]
33	13.574997	–28.439377	0.44741	19.21	134223	80	11.4	K–H–G–Hβ
34	13.573913	–28.442855	0.63013	20.63	189039	87	7.9	K–H–Hδ–G
35	13.571781	–28.435423	0.44862	20.26	134586	73	9.8	H9–K–H–G–Hβ

Figure 6 shows the R-magnitude histogram of the galaxies with measured redshifts superimposed on the magnitude histogram of all galaxies in our pencil beam, indicating that our observations sample uniformly at a rate of 50%–60% of the population of galaxies down to $R = 22.5$. The sampling seems fairly representative in the magnitude bin $R = 22.5 - 23.0$, and sparse at $R > 23$. The apparent increase in incompleteness toward brighter magnitudes is due to a selection bias in the observations, which were designed to avoid bright galaxies at redshifts $z \leq 0.25$.

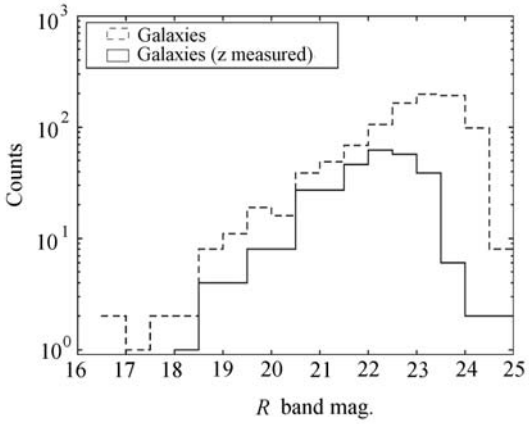

Fig. 6 R-magnitude histogram of galaxies with measured redshift in the central beam.

Figure 7 presents the magnitude redshift relation and the cone diagrams for the full sample. The points are color coded according to the presence or absence of emission lines.

A cursory inspection of Figure 7 reveals the presence of several conspicuous structures - walls of objects spanning almost the entire field of view - over the full range of redshifts covered by our observations. Ignoring objects with $z < 0.28$, we see structures centered at $z = 0.29$ (our prime target); two distinct structures at $z \sim 0.4$, which we will denote $z = 0.415$ and $z = 0.447$; a rather complex structure at $z \sim 0.6$, with two main overdensities at $z = 0.58 - 0.63$ and $z = 0.68$; and a single rather sparsely populated layer at $z = 0.82$. In what follows, we will refer to these groups (including the main cluster at $z = 0.29$) as our pencil beam structures. Centering the bins on the peaks of the redshift distribution maximizes the number of objects in each bin and minimizes its redshift dispersion. So using the apparent structures rather than a blind slicing appears well-suited to our sample. If the structures are real, the objects of a given structure may have a common history and this may also help to reduce the cosmic scatter.

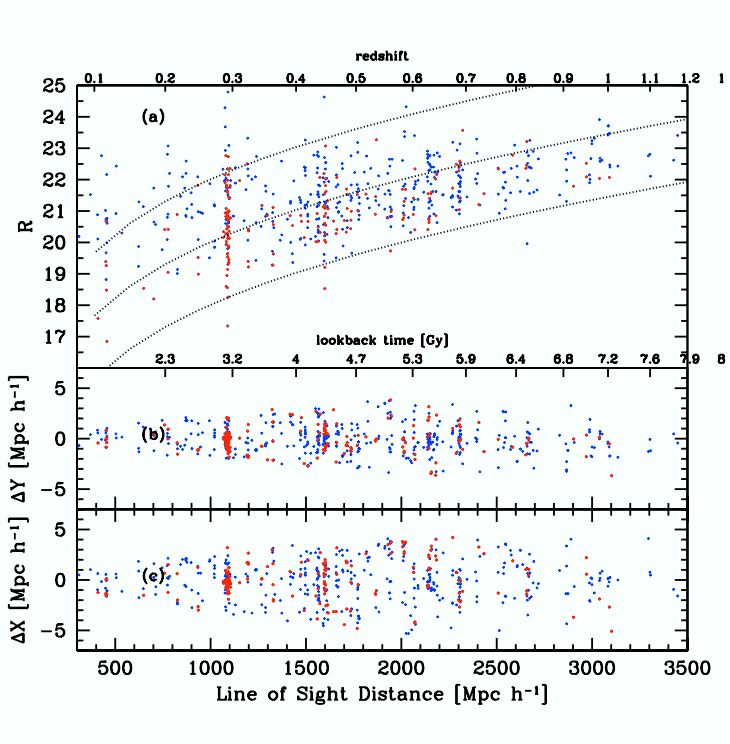

Fig. 7 (a) Magnitude redshift relation for the full sample. The three lines plotted over the measured points correspond to absolute R magnitudes of –22.5, –20.5 and –18.5. The distances have been calculated using a cosmology with $\Omega_{0,\Lambda} = 0.70$, $\Omega_{0,m} = 0.30$, $w = -1$ and $H_0 = 75\,\mathrm{km\,s^{-1}\,Mpc^{-1}}$ ($h = H_0/75\,\mathrm{km\,s^{-1}\,Mpc^{-1}}$). Red dots are galaxies with no emission lines and blue dots are galaxies with emission lines. (b) Cone diagrams in Dec for all the galaxies measured in the field of RX J0054.0–2823. The scales are in Mpc, calculated using the angular distance for the standard cosmology. The detection threshold for emission lines is EQW([OII])$\sim 2-3$ Å. (c) Same as (b) but for RA.

The numbers of spectra observed in each structure are given in Table 6. The redshift bins given in Col. (2) are chosen *a posteriori* to fit the structures. The numbers of redshifts measured in each bin are given in Col. (3), with the respective numbers of absorption and emission systems in Cols. (4) and (5). We have determined the median distance to the nearest object $\Delta\delta$ in each of the apparent structures in Col. (6), and the median velocity dispersion, $\sigma(V) \equiv c\sigma(z)/(1+z)$, in Col. (7). We give a rough morphology of the structures in Col. (1). The cluster at $z = 0.293$ appears to have a small projected separation and velocity dispersion. Layers or filaments have a comoving velocity dispersion (dynamical and cosmological) less than $\sim 1500\,\mathrm{km\,s^{-1}}$; clouds have $\sigma(V) > 2000\,\mathrm{km\,s^{-1}}$. The structures marked "filaments" are the arc layers seen in Figure 7. Projected on the sky, they seem to be filamentary, but the median distances $\Delta\delta$ to the nearest object are approximately 2/3 those expected for uniform distributions, so they are not clearly different from the 2D layers. The names of the bins that are used to combine spectra are given in Col. (8). Large scale arc structures, as seen in the cone diagrams, are expected to be formed by the infall of galaxies due to gravitational potentials: galaxies which are on the far side have a negative infall velocity, while those on the near side have a positive infall component, which when superimposed on the Hubble flow reduces the

Table 6 Apparent Structures in the Field of RX J0054.0–2823

Apparent Structure (1)	z range (2)	N (3)	N (abs) (4)	N (em) (5)	$\Delta\delta$ (kpc) (6)	$c\sigma(z)/(1+z)$ (7)	Composite Name (8)
	0.275 – 0.285	0	0	0			
Cluster	0.285 – 0.298	91	60	31	165	527	SPEC029
	0.298 – 0.320	5	1	4			
	0.320 – 0.330	12	7	5			
	0.330 – 0.390	28	7	21			
	0.390 – 0.430	35	6	29	490	3250	SPEC0415
Filament (layer)	0.432 – 0.440	29	5	24	500	350	SPEC0415
	0.440 – 0.444	1	1	0			
Filament (layer)	0.444 – 0.456	46	21	25	470	450	SPEC0447
	0.456 – 0.465	1	1	0			
Cloud	0.465 – 0.550	53	15	38	480	3370	
Cloud	0.550 – 0.620	56	15	41	520	3550	SPEC063
Filament (layer)	0.620 – 0.657	48	12	36	580	1450	SPEC063
	0.657 – 0.673	1	0	1			
Filament (layer)	0.673 – 0.696	43	12	31	650	1010	SPEC068
	0.710 – 0.790	22	4	18			
Filament & cloud	0.790 – 0.850	33	6	27	820	2050	SPEC082
	0.850 – 0.880	0	0	0			
Cloud	0.880 – 0.930	11	1	10			
	0.930 – 0.946	0	0	0			
Cloud	0.946 – 1.046	25	4	21	1080	4110	SPEC099

Table 7 Average R-band magnitudes of absorption systems (abs), and red and blue emission line galaxies. The adopted distance moduli $(m - M)_0$ and the 4150–4250 Å fluxes f normalized to the blue galaxies at $z = 0.9$ are also tabulated.

$\langle z \rangle$	R (abs)	R (red)	R (blue)	$(m - M)_0$	f (abs)	f (red)	f (blue)
0.29	19.80	20.12	20.97	40.18	0.74	0.72	0.48
0.43	20.24	20.59	20.95	40.86	1.08	0.92	0.75
0.65	21.50	21.60	21.94	41.51	1.42	1.28	0.86
0.9	22.45	22.13	22.35	41.98	2.08	1.70	1

velocity dispersion. This is presumably what we observe in the two filaments or layers with low velocity dispersion at $z = 0.4$.

We combined the spectra in each structure using the median. This results in a slightly lower total S/N (by $\sqrt{2}$), but allows us to eliminate spurious features.

3.1 Magnitudes

The R-band average magnitudes of galaxies in each redshift bin are given in Table 7 separately for absorption and "red" and "blue" emission line galaxies, together with the adopted distance moduli. The partition "red" versus "blue" is defined by the median spectral slope in each redshift bin. In a study of emission line galaxies (Giraud et al. 2010), we divided the sample of emission line galaxies into two halves: those with continuum slopes bluer than average and those with continuum slopes redder than average in each redshift bin. This was done interactively by displaying reduced 1D spectra and using MIDAS. While a median partition is not necessarily a physical partition, we showed that, in the present case, it divides "young" galaxies, for which the evolution is dominated by ongoing star formation, from "old" galaxies, where the evolution is dominated by changes in the older stellar populations.

We used the R-band photometry to calibrate individual spectra by convolving each spectrum with a box filter 1290 Å wide, centered at $\lambda = 6460$ Å. Once the spectra were calibrated in the observer's R-band, we measured the average fluxes in the wavelength range 4150–4250 Å of the galaxies, which we normalized to the flux of blue emission galaxies at $\langle z \rangle = 0.9$ to compute the luminosity index f. Thus, f (which is equal to 1 for blue galaxies at $\langle z \rangle = 0.9$) is an indicator of AB(4200) that allows us to compare the luminosities of red and blue galaxies at a given redshift and to investigate luminosity variations with z. Table 7 clearly shows that in each redshift bin, absorption line and red emission line galaxies are more luminous than blue galaxies.

4 COMPOSITE SPECTRA

Each galaxy spectrum was wavelength calibrated, corrected for instrument response, re-binned to zero redshift, and normalized to have the same flux in the wavelength range $\Delta\lambda = 4050 - 4250$ Å. Normalizing spectra gives the same weight to all galaxies. As a consequence, stellar fractions must be understood as average stellar fractions per galaxy.

We have truncated the sample at $z = 1.05$ and assembled the spectra in bins centered on (pseudo) structures at 0.29, 0.41, 0.45, 0.63, 0.68, 0.82 and 0.99 to build high S/N composite spectra for each bin. In order to compensate (or at least minimize) Malmquist bias, we rejected objects fainter than $M_R = -18.8$, which are mostly at $z \leq 0.45$ (Fig. 7(a)). A sample completely free of Malmquist bias would require a cutoff at $\mathrm{M_R} \sim -20.5$. For clarity in the figures, we often combined the mean spectra at $z = 0.41$ and 0.45 into a single bin at $\langle z \rangle = 0.43$, the spectra at $z = 0.63$ and 0.68 into a bin at $\langle z \rangle = 0.65$, and in some cases the spectra at $z = 0.82$ and 0.99 into a bin at $\langle z \rangle = 0.9$. The spectra of galaxies in these four bins are presented in Figure 8, where we separately show the spectra of absorption systems (left) and emission line galaxies (right). The corresponding 4000 Å break amplitudes are given in Table 8.

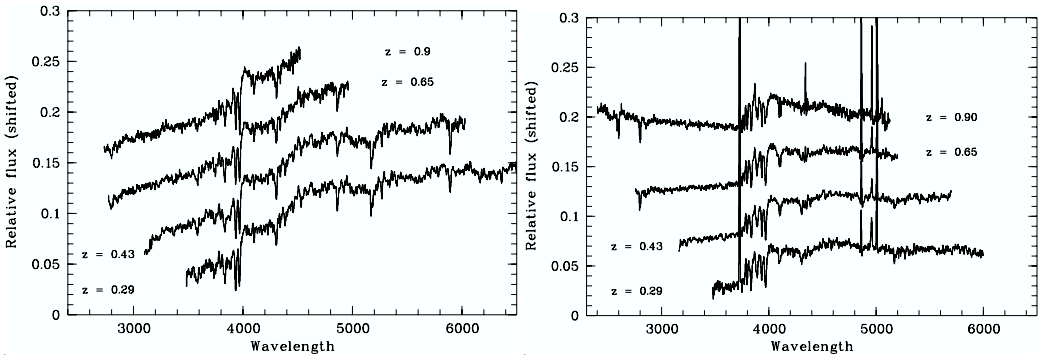

Fig. 8 Composite spectra of absorption systems (*left*), and emission line galaxies (*right*) normalized in the wavelength range $\Delta\lambda = 4050 - 4250$ Å. All individual galaxies are brighter than $M_R = -18.8$.

The most conspicuous spectral change with redshift is a decrease in flux redward of the G-band from $\langle z \rangle = 0.29$ and $\langle z \rangle = 0.43$ redshift bins to higher z coupled with an increase to the blue of [OII] from the $\langle z \rangle = 0.65$ redshift bin to that at $\langle z \rangle = 0.82$ and higher z in emission line galaxies. This systematic change of the continuum implies that the galaxy population varies as a function of redshift: more star forming galaxies at higher z and more galaxies with old stars at lower z. This spectral change, which is well-known, will not be studied further in this paper except to quantify (in 5.3.1) the impact of LINER-like galaxies at $z = 0.4 - 0.9$. In the following section, we concentrate on absorption systems and low-ionization galaxies.

Table 8 4000 Å break amplitudes for absorption (abs) and emission (em) galaxies, and equivalent widths of Hδ for absorption galaxies with measurement errors. The S/N ratios of the combined spectra were measured in the interval 4050 Å–4250 Å. The magnitude cutoff is $M_R = -18.8$ for all redshift bins.

	Absorption systems			Emission systems	
$\langle z \rangle$	D(4000)	EQW(Hδ)	S/N	D(4000)	S/N
0.29	1.67 ± 0.065	-1.5 ± 0.2	23	1.22 ± 0.02	32
0.43	1.70 ± 0.06	-1.5 ± 0.2	22	1.22 ± 0.01	52
0.65	1.60 ± 0.055	-1.8 ± 0.2	24	1.14 ± 0.01	35
0.82	1.57 ± 0.06	-2.4 ± 0.5	18	1.07 ± 0.02	28
0.99	1.43 ± 0.05	-2.9 ± 0.3	23	1.08 ± 0.02	25

5 ABSORPTION LINE SYSTEMS

The spectral resolution of the 300V grism allows us to detect [OII] emission down to EQW([OII])$\sim 2 - 3$ Å. We will call absorption line galaxies those for which any mechanism of ionization is low enough to preclude [OII] detection at our detection level. Thus, our pure absorption line sample comprises mostly E, E+A and S0 galaxies, with no on-going star formation, nuclear activity, or other mechanism of ionization.

5.1 Absorption Systems as a Function of Redshift

The normalized and combined spectra of absorption line systems presented in Figure 8 (left) do not show any obvious change in their continuum and 4000 Å break amplitude up to $z \approx 0.6$ (Table 8). There is a moderate decrease in the 4000 Å break at $z \geq 0.65$ ranging from 5% at $z \sim 0.65$ to 7% at $z \sim 0.82$ and up to 15% at $z \sim 1$, while the Hδ absorption line becomes stronger at $z \geq 0.65$ (Table 8), suggesting the presence of increasing numbers of A stars at higher redshifts. The indexes suggest that these galaxies had the bulk of their star formation at $z \geq 1$, while some of the systems at $z > 0.8$ still had clearly detectable star formation about 1 Gyr ago.

We have compared our spectral indexes at $z \sim 0.82$ with those measured by Tran et al. (2007) in the rich cluster MS 1054–03 at $z = 0.83$ using the same index definitions from (Kauffmann et al. 2003). The average break amplitude and Hδ index of absorption systems in MS 1054–03 are respectively $\mathrm{D}(4000)(\mathrm{abs}) = 1.67 \pm 0.00$ and EQW(Hδ) (abs) = -1.7 ± 0.0 (Tran et al. 2007, table 4). Our absorption systems at $z \sim 0.82$ appear to have younger stellar populations as indicated both by $\mathrm{D}(4000)$ and EQW(Hδ) (Table 8). Therefore, our absorption systems contain A stars, but clearly less than composite field E+A galaxies at $\langle z \rangle = 0.6$ for which $\mathrm{D}(4000)(\mathrm{abs}) = 1.36 \pm 0.02$ and EQW(Hδ) (abs)=-4.6 ± 0.2 (quoted in Tran et al. (2007, table 4) from data in Tran et al. (2004)). Consequently, our average spectrum at $z \sim 0.82$ is intermediate between pure E and pure E + A. In fact, our SSP models (Table 9) indicate that absorption line systems at $z \geq 0.65$ contain on average more than 50% of stars younger than 2.5 Gyr per galaxy, while those at $z \geq 0.8$ had significant star formation as recently as one Gyr ago (Table 9).

Post-starburst E+A galaxies are thought to be in a transition phase between a star-forming period and a passively evolving period. Being close to the phase of shutdown or *quenching* of star formation, they probably play an important role in the build-up of early-type systems (e.g. Wild et al. 2009; Yan et al. 2009). Studies of intermediate redshift clusters at $0.3 \leq z \leq 0.6$ have found either a higher fraction of post-starburst galaxies in clusters than in the field (Dressler et al. 1999; Tran et al. 2003; Tran et al. 2004), or a similar fraction (Balogh et al. 1999). In fact, there is a strong variation in the E+A fraction between the SSDS low redshift survey at $z \sim 0.07 - 0.09$, and high z surveys at $z \approx 0.5 - 1$ (VVDS, Wild et al. 2009), or $z \approx 0.7 - 0.9$ (DEEP2, Yan et al. 2009).

Table 9 Stellar population properties of normalized average absorption (abs) spectra in each redshift bin. The magnitude cutoff is at $M_R = -18.8$, except for the ten faintest absorption systems at $z = 0.29$, where we used all the observed objects. The fractions indicated in all SSP tables are standard luminosity fractions at 4050 Å, as in Cid Fernandes et al. (2010, and references therein)

$\langle z \rangle$	log (Age)	< 8	$8 - 8.7$	$8.7 - 9$	$9 - 9.4$	> 9.4
0.29	abs	0.0%	0.0%	30.1%	0.1%	69.8%
	abs (10 brightest)	0	0	17.4	0	82.4
	abs (10 faintest)	0	0	12.0	66.4	21.7
0.43	abs	0.0	0.7	11.7	6.9	80.7
0.65	abs	0.0	0.0	18.2	38.5	43.3
0.82	abs	0.0	0.0	86.8	3.3	9.8
0.99	abs	0.0	0.0	42.3	0.0	57.7

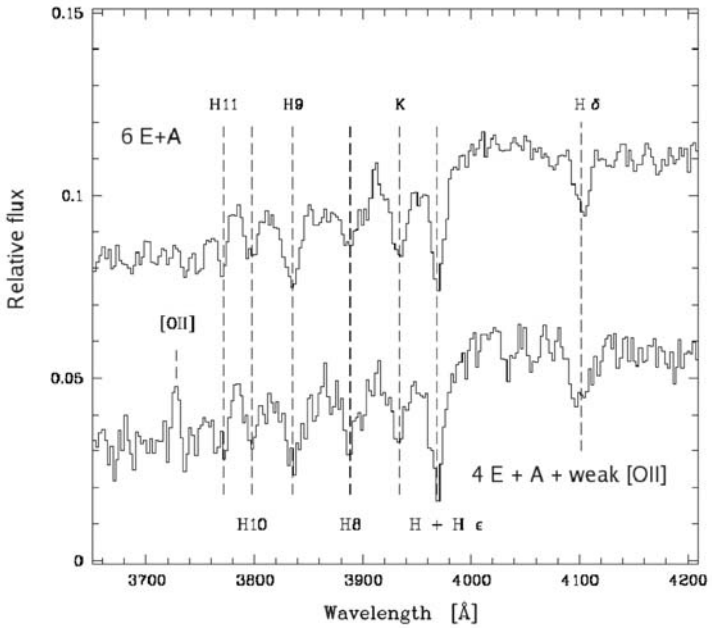

Fig. 9 *Top*: average spectrum of six E+A galaxies at $0.68 \leq z \leq 1$. The Balmer series, including Hδ, H + Hϵ, H8, H9, H10, and H11, is very prominent and $\langle \mathrm{D}(4000) \rangle = 1.40$. *Bottom*: average spectrum of four galaxies in the intermediate redshift range $0.4 \leq z \leq 0.5$ with E/S0 morphological type, showing a post-starburst E+A spectrum still showing some star formation. $\langle$EQW([OII])$\rangle \approx 3.5$ Å and $\langle \mathrm{D}(4000) \rangle = 1.41$. Probably, this spectrum would have been classified as E+A at lower resolution.

In order to search for E+A galaxies in our sample, we built template spectra by combining a pure E spectrum from our sample with various fractions of an A stellar template. We then compared our models with absorption line systems in the range $1.2 \leq \mathrm{D}(4000) \leq 1.5$ assuming, by definition, that E+A galaxies contain at least 25% A stars. Using this (standard) definition, we searched our sample at $0.35 \leq z \leq 1$ and found only six bona fide E+A galaxies. In fact, all the objects were found at $0.68 \leq z \leq 1$, which makes our small number be consistent with the VVDS and the

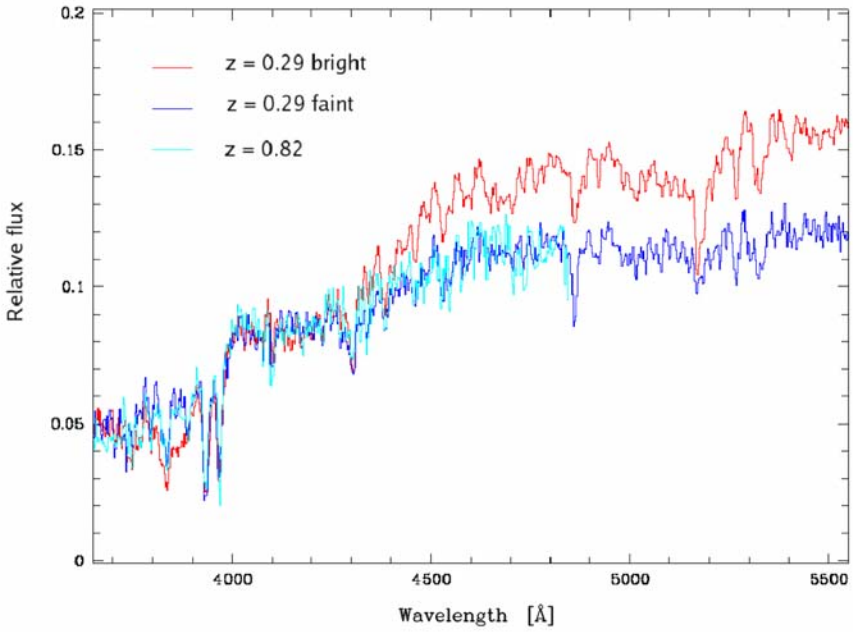

Fig. 10 Normalized spectra of the ten brightest (in red) and the ten faintest (in blue) absorption line galaxies in the cluster at $z = 0.29$, and the full sample of absorption line systems at $z = 0.82$ (in cyan, *color online*).

DDEP2 surveys within a factor of two. The median of the normalized spectra of these six (as far as we can judge from our images) elliptical galaxies is presented in Figure 9 (top). We were surprised to find no E+As at $z \sim 0.4$, but we did find four objects with early-type morphology and very small $\langle \mathrm{EQW([OII])} \rangle \approx 3.5$ Å, which probably would have been classified as E+As in lower resolution spectra. The average spectrum of these four objects is shown in Figure 9 (bottom). Their $R \sim 22$ magnitudes place them at the faint end of the absorption line systems at the corresponding redshifts.

5.2 Absorption line Galaxies as a Function of Luminosity at $z = 0.29$

Having tested bright absorption galaxies at various redshifts (with cut-off at $M_R = -18.8$), we now turn to faint absorption galaxies in the cluster at $\langle z \rangle = 0.29$ by combining the spectra of the ten faintest galaxies without emission lines. Their average R-band magnitude is $R = 22$, which at a distance modulus of 40.18 corresponds to $M_R = -18.2$, and the faintest object has $M_R = -17.44$. Their mean indexes, $\mathrm{D}(4000) = 1.55 \pm 0.01$ and $\mathrm{H}\delta = -2.27 \pm 0.04$, measured on the spectrum shown in Figure 10, are consistent with a younger age than absorption line galaxies with $M_R \leq -18.8$ (Table 8) in the same cluster. This is in agreement with the well known evidence that the stellar populations in absorption systems tend to be younger in low mass galaxies than in the more massive ones (e.g. Renzini 2006). The index values are in fact very close to those of our absorption systems at $z = 0.8$ (Table 8) which, by selection effects, are bright (Table 7 and Fig. 7).

The SSP models indicate that on average about 80% of the stars in the ten faintest galaxies are younger than 2.5 Gyr (Table 9), i.e. were born at $z < 1$. In comparison, 80% of the stars contributing to the spectrum of the brightest absorption galaxies in the cluster are older than 2.5 Gyr (Table 9).

To illustrate the spectral differences between bright and faint systems at $z = 0.29$, and the striking similarity between the spectra of faint galaxies at $z = 0.29$ and those of bright galaxies at $z = 0.8$, we have plotted in Figure 10 the average spectra of the ten brightest and the ten faintest absorption systems at $z = 0.29$, and the average spectrum of absorption galaxies at $z = 0.82$. The effect of *downsizing*, (in the present case, the so-called 'archeological downsizing') where star formation shifts from high mass galaxies at high redshifts to low mass galaxies at low redshifts, is clearly exemplified in this figure.

At a redshift of $z \sim 0.8$ (i.e. ~ 4 Gyr earlier), the red-sequence of our unrelaxed (merging central system; elongated intra-cluster light and galaxy distribution) cluster at $z = 0.29$ was already in place, but was truncated at brighter magnitudes because the faint absorption line galaxies were still copiously forming stars. This seems to be consistent with the observation that some clusters at $z \simeq 1$ have red sequences truncated at faint limits (Kodama et al. 2004; Koyama et al. 2007), and supports the picture of an environmental dependence of red-sequence truncation presented by Tanaka et al. (2005). This is also in agreement with scenarios where the final assembling of the red-sequence can be observed well below $z = 1$ (Faber et al. 2007).

As discussed above, the strict definition of an E+A galaxy requires a mix of an E-type spectrum with at least 25% A stars and no traces of star formation, which in our sample implies no emission lines with equivalent widths larger than 2–3 Å. With this definition, our $z = 0.29$ cluster contains only one E+A galaxy while the dense layers at $z \sim 0.4$, where the red-sequence is already in place (layer in Fig. 7), contains none. However, both in the cluster and in the intermediate redshift layers, we find plenty of galaxies with early type morphologies, A stars, and very weak emission lines. In the next section, we present a closer look at these low-ionization emission line galaxies.

5.3 Galaxy Evolution and Low-ionization Emission line Galaxies (LINERs).

In an extensive work based on the SDSS survey, Yan et al. (2006) determined the extent to which [OII] emission produced by mechanisms other than recent star formation introduces biases in galaxy evolution studies only based upon [OII]. They showed that the $[\mathrm{OII}]/\mathrm{H}\beta$ ratio separates LINERs from star-forming galaxies, while $[\mathrm{OIII}]/[\mathrm{OII}]$ and $[\mathrm{OIII}]/\mathrm{H}\beta$ separate Seyferts from LINERs and star-forming galaxies. Using the classification scheme of Yan et al. (2006), we divided our spectra into two main classes: LINERs, with clearly detected [OII], but no (3σ) detection of [OIII] and $\mathrm{H}\beta$ in emission after subtracting an E+A profile; Seyferts, with $[\mathrm{OIII}]/\mathrm{H}\beta \geq 3$, and star-forming galaxies, which are the objects with clearly detected [OII] that are neither Seyferts nor LINERs after subtracting an E+A profile. Typical spectra of low-ionization objects, star-forming galaxies and Seyferts are shown in Figure 11.

5.3.1 The impact of LINERs in our previous results on red emission line galaxies

Because the spectral coverage in a rather large fraction of our objects at $\langle z \rangle = 0.68$ and higher is truncated below 5000 Å in the rest frame, we applied our classification scheme only to objects in the range $0.29 \leq z \leq 0.65$. To extract $\mathrm{H}\beta$ in emission, we built a series of E+A models, combining an observed E spectrum with different fractions of an A stellar template, ranging from 0.05% to 80% of the total luminosity. To determine the best-fit model, we minimized the continuum slope of the difference between the spectrum and the E+A model. Thus, in the range 0.35–0.55, our sample contains 23% LINERs, 51% star-forming galaxies, 8% Seyferts and 14% uncertain types. The layer at $z = 0.63$ has 18% LINERs, 50% star-forming galaxies, 7% Seyferts, 13% uncertain types and 11% truncated spectra. Altogether, the fraction of LINERs among emission line galaxies up to $z = 0.65$ in our pencil beam is $\approx 22\%$. With an average $\langle \mathrm{D}(4000) \rangle = 1.39 \pm 0.18$, LINERs at $z \leq 0.65$ have a potentially significant impact on the conclusions of Giraud et al. (2010) about the evolution of red emission line galaxies. To quantify this impact, we have subtracted all LINERs from the sample

of emission line spectra in the $z = 0.43$ bin, determined the new blue-to-red partition (as in Giraud et al. 2010; sect. 5.1), and computed a new average spectrum for the red galaxies. This (also cleaned of rare red Seyferts) is shown in Figure 12, where it is compared with the mean red spectrum at $z = 0.9$. We find that the differences in continuum slope and D(4000) between $\langle z \rangle = 0.43$ and

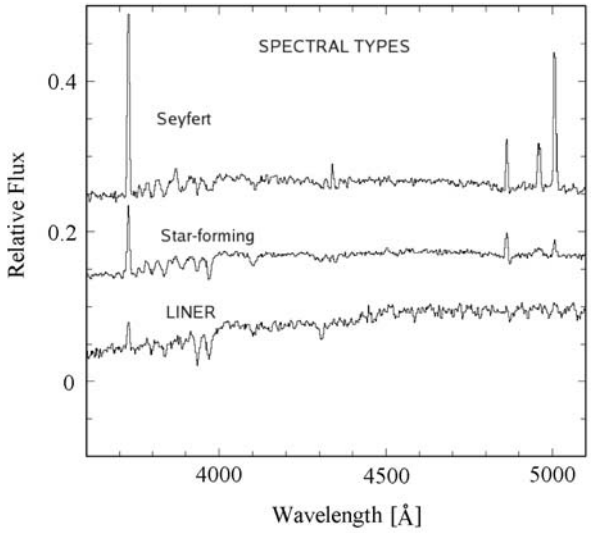

Fig. 11 Typical average spectra of low-ionization objects, star-forming galaxies and Seyferts from the sample in the $\langle z \rangle = 0.415$ layer.

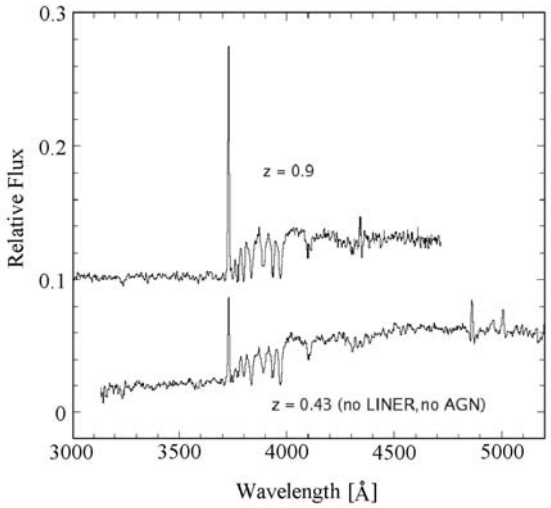

Fig. 12 Average spectra of red emission line galaxies after subtracting early-type LINERs and galaxies with diluted star formation (and rare Seyferts) from the sample in the $\langle z \rangle = 0.43$ bin and recalculating the median blue-to-red partition, and of the red half of emission line galaxies at $\langle z \rangle = 0.9$. The spectra at $\langle z \rangle = 0.9$ were not classified because Hβ and [OIII] are missing in most cases.

$\langle z \rangle = 0.9$ is reduced by a factor of 2/3. The main difference between red galaxies with LINERs and those without is the presence of a young stellar population.

5.3.2 Early-type LINERs

The fraction of nearby early-type galaxies hosting bona fide (i.e. nuclear) LINERs in the Palomar survey (Filippenko & Sargent 1985; Ho et al. 1997a) was found to be $\sim 30\%$ (Ho et al. 1997b), but LINER-like emission line ratios are also observed in extended regions (Phillips et al. 1986; Goudfrooij et al. 1994; Zeilinger et al. 1996; Sarzi et al. 2006, and references therein). A similar fraction of LINER-like ratios is found in the SDSS at $0.05 \leq z \leq 0.1$ in color-selected red galaxies (Yan et al. 2006).

Because it is very difficult to disentangle early-type LINERs from spirals with extended and diluted star formation by using only [OII] and Hβ, we make use of morphology to distinguish compact objects with low ellipticity and profiles consistent with early type galaxies, from other morphologies: apparent disks, high ellipticity, and irregular or distorted morphologies. Images of early-type galaxies with low ionization spectra are shown in Figure 13.

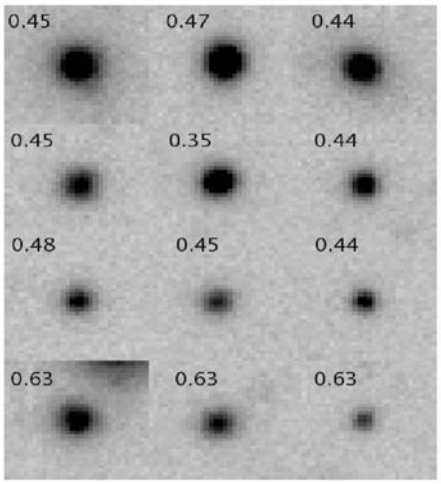

Fig. 13 Examples of early-type galaxies having low-ionization spectra and indicated redshifts.

Our visual early-type morphologies are the same as ZEST type T=1 (Scarlata et al. 2007, figure 4(b), (c), (d)). In the $\langle z \rangle = 0.43$ bin, we find that 92% of the galaxies classified as star-forming objects have morphologies inconsistent with early-types. At $\langle z \rangle = 0.43$ and in the $z = 0.63$ layer, about half of the LINERs have compact morphology while the other half are mainly bulge-dominated disk galaxies, or "early disks" of ZEST type $T = 2.0$ (Bundy et al 2010, fig. 4). At $z = 0.29$, all LINERs have disks. The spectra of galaxies with apparent disks have an extended [OII] emission suggesting that they do have extended star-formation. Average spectra of 11 early-type galaxies (E) and 10 later types (hereafter S) resulting from our morphological classification are shown in Figure 14.

The absence of Hβ in the S sample suggests that Hβ in emission resulting from star formation is diluted in Hβ in absorption from A and older stars. The closest spectral comparison in the atlas of galaxy spectra (Kennicutt 1992) is with an Sb galaxy. The rather strong Hβ in absorption in early-types (E) combined with [OII] suggests either a low fraction of young stars or a mechanism of photo-

ionization other than young stars, as in Fillipenko (2003), Ho (2004), and references therein. In fact, the recent work by the SEAGAL collaboration (Cid Fernandes et al. 2010, and references therein) has shown that the majority of galaxies with LINER spectra in the SDSS can be explained as *retired galaxies*, that is, galaxies that have stopped forming stars but still contain appreciable amounts of

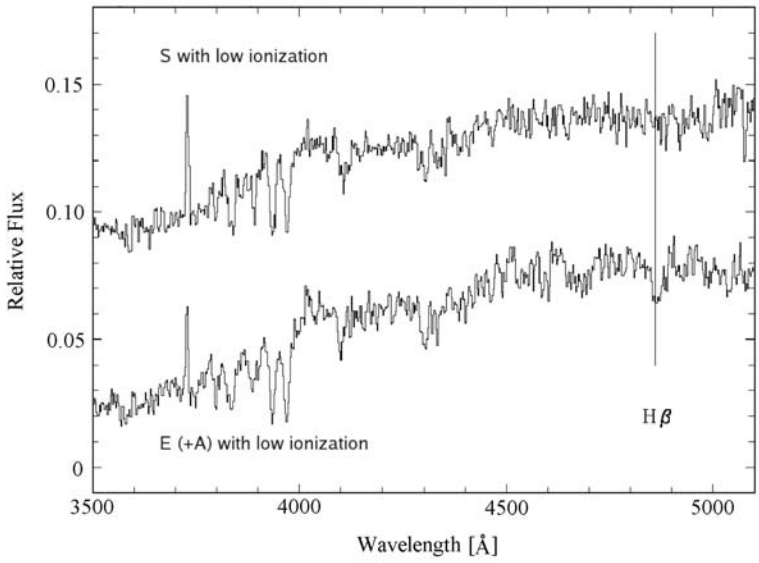

Fig. 14 Median spectra of 11 early-type galaxies and of 10 galaxies with late-type morphology (S) with low ionization at $z = 0.4 - 0.5$.

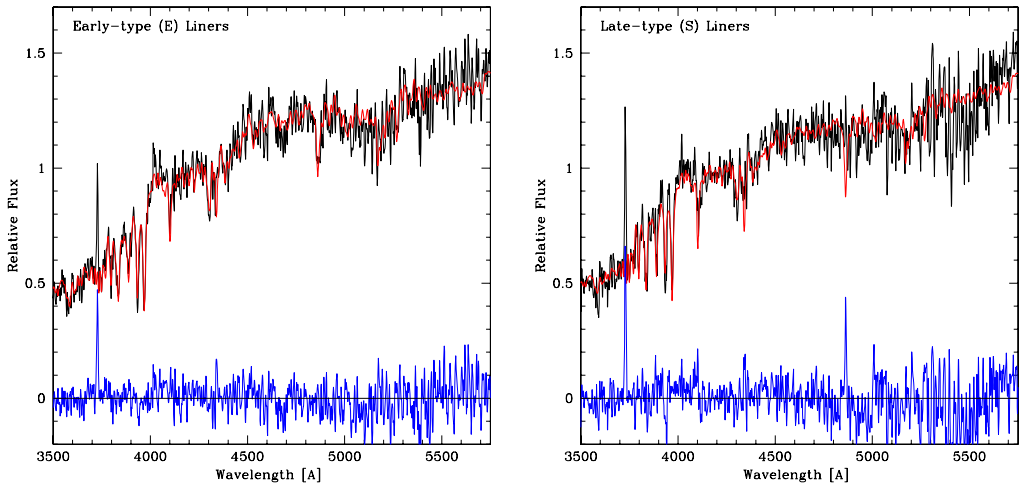

Fig. 15 Spectral fitting with SSP models for an average spectrum of LINERs with early-type morphology (*left*), and with morphology of later type (*right*).

Table 10 Stellar Population Properties of an Average of LINERs with Early-type Morphology and with Morphology of Later Types

Type	log Age					χ^2
	< 8	$8 - 8.7$	$8.7 - 9$	$9 - 9.4$	> 9.4	
Early	18.2	0	57.6	0	24.2	1.4
Later-type	32.7	0	53.4	0	13.9	1.3

gas that is being photoionized by intermediate-aged post-AGB stars. In fact, the SEAGAL models with no young stars, but with significant populations of 100 Myr – 1 Gyr stars resemble remarkably well our average LINER spectrum shown in Figure 11.

We calculated population synthesis models for our average spectra of LINERs with early-type and late-type morphologies. The results, shown in Figure 15 and Table 10, indicate that both early-type and late-type LINERs have significant populations of young and intermediate age stars, but late-type (S) LINERs have much younger populations. In fact, the residuals of the S-LINER fit show Hβ in emission stronger than [OIII], consistent with the idea that they are red spirals with diluted star formation.

Thus, our results are consistent with the interpretation that most early-type LINERs at intermediate redshifts are in fact post-starburst galaxies, as postulated by the SEAGAL collaboration for lower redshift objects. These results indicate that LINERs and E+As depict the quenching phase in the evolution of galaxies massive enough to retain significant amounts of gas after the stellar-wind and supernova phases of the most massive stars.

5.4 The Red Limit of Emission line Galaxies

At each z, we have selected galaxies with the reddest continuum (the reddest quartile at each redshift bin) to construct the combined spectra of the red envelope or red limit of emission line galaxies. Since we are working with small numbers of galaxies, typically 5–10, it was necessary to combine the samples at $z = 0.82$ and $z = 0.99$ to improve statistics. Nevertheless, because our red emission line galaxies are rather luminous, the combined spectra still have high continuum S/N ratios (Table 11).

Table 11 Equivalent width of [OII], 4000 Å break amplitude, Hδ index, and the G-step of the red envelope of emission line galaxies. The continuum S/N ratios are given in the last column.

$\langle z \rangle$	EQW([OII])	D(4000)	EQW(Hδ)	G step	S/N
0.29	4.2 ± 0.3	1.35 ± 0.07	-1.8 ± 0.3	1.224 ± 0.017	19
0.43	8.5 ± 0.2	1.39 ± 0.06	-2.5 ± 0.2	1.268 ± 0.014	24
0.65	8.3 ± 0.2	1.44 ± 0.06	-3.0 ± 0.2	1.273 ± 0.012	29
0.9	9.0 ± 0.3	1.30 ± 0.07	-3.9 ± 0.2	—	18

The common parts of the red envelopes of spectra at $\langle z \rangle = 0.29$, $\langle z \rangle = 0.43$, and $\langle z \rangle = 0.65$ are similar, but the red limit at $\langle z \rangle = 0.9$ has a noticeably stronger UV continuum. The spectra in different bins are shown in figure 7 of Giraud et al. (2010). Both the continuum and the indexes of the red limit at $z \leq 0.65$ (i.e. $\mathrm{D}(4000) \sim 1.35 - 1.45$, EQW([OII])$\sim 4 - 8$) are typical of nearby spirals with prominent bulges and low star formation (Kennicutt 1992; Kinney et al. 1996; Balogh et al. 1999), or early-type LINERs. Up to $z \sim 0.7$, the populations of red spirals and early-types can be well separated by their morphology. The higher UV continuum and lower $\mathrm{D}(4000)$ of the limit spectrum at $\langle z \rangle = 0.9$ indicate that such red objects become rare at $z \geq 0.68$ in our sample.

Absorption systems have (by definition) already lost enough gas to suppress any detected star formation by the time they first appear in our sample at $z \simeq 1$. At $z = 0.8 - 1$, emission line galaxies in our sample are found to have very strong star formation, which declines at lower z, with

the reddest quartile being bluer than at lower z. Therefore, the evolutionary paths of bright absorption and emission systems might have been more separated at $z \simeq 1$ than at lower redshift, suggesting two different physical processes with different time scales. In one, we have early-type LINERs and E+A galaxies that define the "entrance gate" to the red sequence of passively evolving galaxies. In the other, we have red spirals with diluted star formation, that are in a final phase of smooth star formation, possibly of a "main sequence" (Noeske et al. 2007).

In Section 5.3, we found a large fraction of LINERs in layers at intermediate z. More precisely, in the volume-limited range $0.35 \leq z \leq 0.65$, we find, gathering the counts of Section 5.3, that LINERs are 23% of all early-type galaxies with measured redshifts.

6 SUMMARY AND CONCLUSIONS

We have presented a catalog of galaxy spectra in a pencil beam survey of $\sim 10.75' \times 7.5'$, and used these data to make an analysis of the spectral energy distribution of a magnitude limited sample up to $z \sim 1$, concentrating on absorption and low ionization emission line systems. The redshift range has been divided into bins centered on the structures that were detected in the (RA, Dec, z) pseudo-volume, and corresponding to cosmic time slices of $\sim 1\,\mathrm{Gyr}$. Our sample is reasonably complete for galaxies brighter than $M_R = -18.8$ up to $z \approx 0.5$; at $z \geq 0.75$, the cutoff is at –20.5.

From this analysis, we reach the following conclusions:

1. We confirm in our pencil beam sample the well known result (Hamilton 1985) that absorption line galaxies do not show significant variations in their continuum energy distributions up to $z = 0.6$, and a moderate decrease of the 4000 Å break amplitude of 5% at $z \sim 0.65$, 7% at $z \sim 0.82$, and up to 15% at $z \sim 1$. Using stellar population synthesis models, we find that absorption line galaxies at $z \geq 0.65$ show more than 50% of stars younger than 2.5 Gyr, while those at $z \geq 0.8$ had star formation as recently as 1 Gyr ago. This suggests that the red sequence is still in a buildup phase at $z \leq 1$.
   The faint absorption line galaxies in our dynamically young cluster at $z = 0.29$ have indexes similar to those of bright absorption line systems at $z = 0.8$, suggesting that faint galaxies without emission lines tend to be younger than more massive galaxies with similar spectra. Our population synthesis models indicate that about 50% of the stars contributing to the luminosity of faint absorption line galaxies at $z = 0.29$ were formed at $z < 1$. This is consistent with cases of truncated red sequences observed in some high-z clusters and suggests that clusters with truncated red-sequences may be dynamically young.
2. Combining simple emission line diagnostics with galaxy morphology, we identify a significant population of early-type LINERs at $0.35 \leq z \leq 0.65$. In that redshift range, early-type LINERs constitute about 23% of all early-types galaxies, a much larger fraction than E+A post-starburst galaxies. However, our population synthesis models show that early-type LINERs contain substantial populations of intermediate age stars that can easily explain the observed line emission, as recently proposed by Cid Fernandes et al. (2010). This led us to conclude that most LINERs in our sample are in fact post-starburst galaxies.
3. The red limit in the spectral energy distribution of emission line galaxies at $z \leq 0.65$ is typical of bulge-dominated spirals with moderate star formation, and of early-type LINERs. Thus, early-type LINERs and E+As define the "entrance gate" of the red sequence of passively evolving galaxies, while bulge-dominated spirals have diluted star formation.

Acknowledgements EG thanks the hospitality of ESO and Universidad Catolica in Santiago during the initial phase of this work. JME thanks the hospitality of Nanjing University during the initial phase of this research. Q. Gu would like to acknowledge financial support from the China Scholarship Council (CSC), the National Natural Science Foundation of China (Grant Nos. 10878010, 10221001 and 10633040), and the National Basic Research Program (973 program,

No. 2007CB815405). HQU thanks the partial support from FONDAP "Centro de Astrofísica." PZE acknowledges a scholarship from CONICYT. We thank S. di Serego Alighieri for reading a preliminary version of the manuscript and for his suggestions, and R. Cid Fernandes for fruitful discussions.

References

Baldwin, J. A., Phillips, M. M., & Terlevitch, R. 1981, PASP, 93, 5
Balogh, M. L., Morris, S. L., Yee, H. K. C., Carlberg, R. G., & Ellingson, E. 1999, ApJ, 527, 54
Bell, E. F., et al. 2005, ApJ, 625, 23
Blake, C., et al. 2004, MNRAS, 355, 713
Bruzual, G., & Charlot, S. 2003, MNRAS, 344, 1000
Bundy, K., et al. 2010, ApJ, 719, 1969
Cid Fernandes, R., et al. 2004, MNRAS, 355, 273
Cid Fernandes, R., Mateus, A., Sodre, L., Stasinska, G., & Gomes, J. 2005, MNRAS, 358, 363
Cid Fernandes, R., et al. 2010, MNRAS, 403, 1036
Cooper, M. C., et al. 2006, MNRAS, 370, 198
Dickinson, M., Papovich, C., Fergusson, H. C., & Budavari, T. 2003, ApJ, 587, 25
Dressler, A. 1980, ApJ, 236, 351
Dressler, A., & Gunn, J. E. 1983, ApJ, 270, 7
Dressler, A., et al. 1997, ApJ, 490, 577
Dressler, A., et al. 1999, ApJS, 122, 51
Faber, S., et al. 2007, ApJ, 665, 265
Faure, C., Giraud, E., Melnick, J., Quintana, H., Selman, F., & Wambganss, J. 2007, A&A, 463, 833
Filippenko, A. V., & Sargent, W. L. 1985, ApJS, 57, 503
Filippenko, A. V. 2003 in ASP Conf. Ser. 290, Active Galactic Nuclei: From Central Engine to Host Galaxy, 369
Franzetti, P., et al. (the VVDS Team), 2007, A&A, 465, 711
Garilli, B., et al. (the VVDS Team), 2008, A&A, 486, 683
Giraud, E., Melnick, J., Gu, Q. S., et al. 2010, in press
Goto, T. 2007, MNRAS, 377, 1222
Goudfrooij, P., et al. 1994, A&AS, 105, 341
Gu, Q., et al. 2006, MNRAS, 366, 480
Hamilton, D. 1985, ApJ, 297, 371
Hammer, F., et al. 2005, A&A, 430, 115
Ho, L. C. W., et al. 1997a, ApJS, 112, 315
Ho, L. C. W., et al. 1997b, ApJ, 487, 568
Ho, L. C. W., 2004, in Coevolution of Black Holes and Galaxies, 292
Kauffmann, G., et al. 2003, MNRAS, 341, 33
Kennicutt, R. C. Jr. 1992, ApJS, 79, 255
Kinney, A. L., Calzetti, D., Bohlin, R. C., McQuade, K., Storchi-Bergmann, T., & Schmitt, H. R. 1996, ApJ, 467, 38
Kodama, T., et al. 2004, MNRAS, 350, 1005
Koyama, Y., Kodama, T., Tanaka, M, Shimasaku, K., & Okamura, S. 2007, MNRAS, 382, 1719
Lin, L., et al. 2008, ApJ, 681, 232
Melnick, J., & Sargent, L. W. L. 1977, ApJ, 215, 401
Melnick, J., Selman, F., & Quintana, H. 1999, PASP, 111, 1444
Noeske, K. G., et al. 2007, ApJ, 660, L43
Norton, S. A., Gebhardt, K., Zabludoff, A. I., & Zaritsky, D. 2001, ApJ 557, 150
Phillips, M. M., et al. 1986, AJ, 91, 1062
Postman, M., et al. 2005, ApJ, 623, 721

Renzini, A. 2006, ARA&A, 44, 141
Renzini, A. 2007, ASPC, 380, 309
Sarzi, M., et al. 2006, MNRAS, 366, 1151
Scarlata, C., et al. 2007, ApJS, 172, 406
Scoville, N., et al. 2007a, ApJS, 172, 1
Smith, G. P., Treu, T., Ellis, R. S., Moran, S. M., & Dressler, A. 2005, ApJ, 620, 78
Tanaka, M., et al. 2005, MNRAS, 362, 268
Tonry, J., & Davis, M. 1979, AJ, 84, 1511
Tran, K.-V. H., et al. 2007, ApJ, 661, 750
Tran, K.-V. H., et al. 2004, ApJ, 609, 683
Tran, K.-V. H., et al. 2003, ApJ, 599, 865
Weiner, B. J., et al. 2005, ApJ, 620, 595
Weiner, B. J., et al. 2006, ApJ, 653, 1027
Wild, V., et al. 2009 MNRAS, 395, 144
Yan, R., et al. 2009, MNRAS, 398, 735
Yan, R., Newman, J. A., Faber, S., Konidaris, N., Koo, D., & Davis, M. 2006, ApJ, 648, 281
Yang Y., Zabludoff, A. I., Zaritsky, D., & Mihos, J. C. 2008, ApJ, 688, 945
Zeilinger, W. W., et al. 1996, A&AS, 120, 257